
Article:
Gregory, D.A., Campbell, A.I. and Ebbens, S.J. (2015) The Effect of Catalyst Distribution on Spherical Bubble Swimmer Trajectories. Journal of Physical Chemistry C, 119 (27). pp. 15339-15348. ISSN 1932-7455

https://doi.org/10.1021/acs.jpcc.5b03773

THE JOURNAL OF PHYSICAL CHEMISTRY C

Article

pubs.acs.org/JPCC

Effect of Catalyst Distribution on Spherical Bubble Swimmer Trajectories

David A. Gregory, Andrew I. Campbell, and Stephen J. Ebbens*

Department of Chemical and Biological Engineering, University of Sheffield, Mappin Street, Sheffield S1 3JD, U.K.

Supporting Information

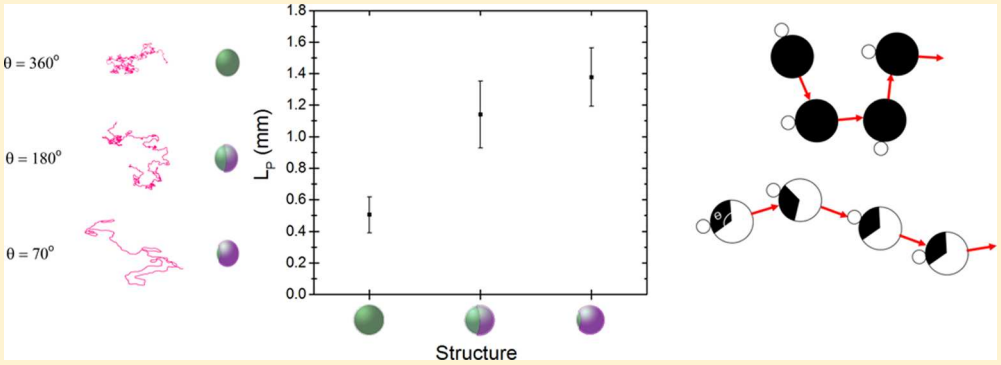

ABSTRACT: Spherical colloids decorated with a surface coating of catalytically active material are capable of producing autonomous motion in fluids by decomposing dissolved fuel molecules to generate a gaseous product, resulting in momentum generation by bubble growth and release. Such colloids are attractive as they are relatively simple to manufacture compared to more complex tubular devices and have the potential to be used for applications such as environmental remediation. However, despite this interest, little effort has been devoted to understanding the link between the catalyst distribution at the colloid surface and the resulting propulsive trajectories. Here we address this by producing colloids with well-defined distributions of catalytic activity, which can produce motion without the requirement for the addition of surfactant, and measure and analyze the resulting trajectories. By applying analysis including fractal dimension and persistence length calculations, we show that spatially confining catalytic activity to one side of the colloid results in a significant increase in directionality, which could be beneficial for transport applications. Using a simple stochastic model for bubble propulsion we can reproduce the features of the experimental data and gain insight into the way in which localizing catalytic activity can reduce trajectory randomization. However, despite this route to achieve trajectory control, our analysis makes it clear that bubble-driven swimmers are subject to very rapid randomization of direction compared to phoretic catalytic swimming devices with equivalent geometries.

1. INTRODUCTION

Producing small-scale autonomous objects capable of moving through fluids, behavior often described as "swimming", has been the subject of considerable attention due to the potential for applications such as drug delivery[1] and other transport functions.[2] Due to restrictions imposed by low Reynolds numbers, autonomous deformation-based swimming, either mimicking flagella-driven bacteria motion or based on more straightforward schemes,[3] has not to date been realized synthetically on the micrometer scale. However, surface catalytic reactions decomposing dissolved fuel molecules have been successfully used to produce a rich variety of autonomously moving devices.[4−7] In many of these examples the catalytic reaction generates a gaseous product (for example, a surface coating of platinum decomposing hydrogen peroxide into water and oxygen), and bubbles can nucleate, grow, and detach from the catalyst-covered regions and produce motion by momentum transfer.[8] Indeed, a range of catalyst distributions, preparation methods, and reactions have been shown to produce bubble propulsion. While complex geometries including rolled up tubes have exhibited bubble propulsion and been subject to intensive research efforts,[9] here we focus on potentially cheaper to produce examples based on introducing catalytic activity at the surface of simple spherical colloids. One early example reported propulsive trajectories, qualitatively described as both linear and rotary, by attaching a synthetic manganese-based catalyst for peroxide decomposition to a spherical silica bead with no spatial control.[10] Later examples have included core/shell colloids, where an inert shell masks the cores' catalytic activity apart from at a well-defined circular pore. In three different published examples (one powered by oxygen bubble generation from a variety of fuels[11] and the other two by hydrogen bubble generation from water using aluminum/gallium[12] and manganese cores[13]) it was qualitatively observed that the inert shell increased the directionality of motion relative to a homoge-

Received: April 20, 2015
Revised: June 10, 2015

DOI: 10.1021/acs.jpcc.5b03773
J. Phys. Chem. C XXXX, XXX, XXX−XXX

neously active core particle alone by localizing the area for bubble generation. However, no trajectory quantification was offered to support and measure this proposed effect. In another example, a dimer was considered, with a bubble-producing lobe (platinum decomposing hydrogen peroxide) attached to an inert polystyrene particle.[14] The dimers were observed to undergo both linear and circular motion depending on the position of bubble nucleation, which appeared to be chaotic. This last study also reported bubble propulsion occurring for spherical particles coated symmetrically in platinum but offered no trajectory comparison between the two structures. Applications for bubble propulsive spherical swimmers have also been investigated, including the ability to detect and photocatalytically degrade biological warfare agents[13] and capture and transport oil droplets,[15] while triggered bubble propulsion in the presence of specific DNA sequences has also been reported as a possible sensor.[16]

Despite this attention and utility, as is apparent from the literature above, the trajectories for spherical bubble swimmers have mainly been only qualitatively described, and the link between surface catalyst distribution and propulsion directionality is poorly understood. In order to further develop these devices, assessing in more detail how catalyst distribution determines the trajectories is desirable, and is consequently the subject of this paper. Surveying the possible methods to characterize bubble swimmer trajectories, it is apparent that mean-square displacement (MSD) versus time trajectory analysis has been used successfully to characterize the trajectories for related Janus colloids which do not produce visible bubbling.[17−19] The lack of bubbling in these smaller catalytic devices is partly due to the energetic cost associated with nucleating bubbles on highly curved surfaces:[20,21] instead motion is thought to be driven by phoretic phenomena. In contrast to bubble propulsion, which has been reported for symmetrical catalyst distributions, an asymmetrical distribution of catalyst has been identified as a key requirement to produce phoretic motion, and video microscopy has established a link between orientation of the catalytic patch and subsequent propulsion direction for nonbubble-producing phoretic swimmers.[22] On the basis of this relationship, analytical theory allows MSD data to be fitted to extract Brownian diffusion parameters and rotational and translational velocities.[23,24] This has allowed the motion of phoretic Janus swimmers at various sizes[23] and agglomerated configurations[25] to be described analytically giving good agreement with experiments. However, the analytical descriptions for MSD versus time evolution that this approach relies on are based on the assumption of an absolute correlation between device orientation and propulsive thrust direction, which has not been established for asymmetrically catalytically active spherical bubble swimmers and is unlikely due to the chaotic nature of surface bubble release. This lack of a simple deterministic model for bubble propulsion renders MSD analysis of limited use for bubble swimmers. For example, MSD plots deviating from the analytical predictions for phoretic swimmers have been proposed as a signature for bubble propulsion,[26,27] but the observed form for the MSD curves has not been explained.

In this context, here we investigate alternative stochastic trajectory analysis methods for bubble swimmers to attempt to establish a quantitative link between catalytic distribution and trajectory. One of the analytical methods applied is persistence length analysis, which has been successful in uncovering features for similar poorly understood stochastic motion observed for protein motor microtubule transport.[28] In addition, we also calculate radius of gyration and fractal dimension. We show that these approaches can successfully distinguish trajectories for spherical bubble swimmers with homogeneous uniform catalytic activity, Janus activity, and activity at a single pore. Using this analysis we show that the catalyst distribution can indeed significantly alter trajectory type for bubble swimmers, but also that the behavior is more complex than the simple relationship observed for phoretic swimmers where an absolute correlation between orientation and propulsion direction exists. Instead, a simple stochastic model for bubble release and device reorientation appears to reproduce the salient features observed for the experimental trajectories.

2. EXPERIMENTAL SECTION

2.1. Particle Preparation. Polystyrene (PS) colloids (30 μm diameter) were uniformly chemically coated with platinum nanoparticles (2−5 nm diameter) by platinum salt reduction to serve as the symmetrical bubble propulsive devices used in this study. In order to mask part of the reactive surface of these particles, colloids were suspended in ethanol solution (99.8% Sigma-Aldrich) and spun cast (Laurell Technologies spin coater) onto precleaned glass slides at volume fractions and coating conditions chosen to ensure the colloids were separate and not touching (as this could cause shadowing effects during masking: verified under an optical microscope). The colloid-covered glass slides were then coated with chromium either via electron-beam-induced thermal evaporation or sputter coating at 5.7×10^{-3} mbar in argon atmosphere (Moorfield combination e-beam/sputter coater). A layer of 300 nm of Cr (99.95% Sigma-Aldrich) was coated onto the particles using these methods, monitored using a quartz crystal microbalance, in near proximity to the colloids. These two masking methods are expected to produce different distributions of the chromium mask due to the difference in the directionality for the two metal deposition protocols.

2.2. Energy-Dispersive X-ray Spectroscopy. In order to view the e-beam and sputter chromium-coated platinum nanoparticle-covered PS colloids from different angles, the colloids were detached from their original substrates using a dry piece of lens tissue by wiping this carefully over the glass slide and then subsequently wiping the colloid-covered tissue carefully over a carbon sticky pad. In this way high contrast for the colloid versus the background was ensured and good attachment of the colloids to the substrate was achieved. Energy-dispersive X-ray spectroscopy (EDS) imaging was performed using a JEOL JSM-6010LA SEM system at an acceleration voltage of 15−18 keV over a period of 40 min per scan (size 512 × 512 pixel).

2.3. Video Microscopy plus Trajectory Analysis. The 30 μm diameter size of the particles considered here allowed them to be imaged in a Petri dish with a diameter of 3 cm and ∼1 cm volume depth that was illuminated with a powerful cold white (BridgeLUX) LED from an ∼45° side angle. This angle ensured that the bubbles produced from the particles left a bright reflection in the imaging camera, which helped to achieve subsequent automatic position tracking. A long distance macrolens was directly mounted onto a PixeLink camera, and 1000 frame long movies were taken at a frame rate of 25 frames/s. During the experiment it was ensured that the room temperature (20 °C) was carefully monitored and air movement and vibrations were kept to a minimum to minimize

DOI: 10.1021/acs.jpcc.5b03773
J. Phys. Chem. C XXXX, XXX, XXX−XXX

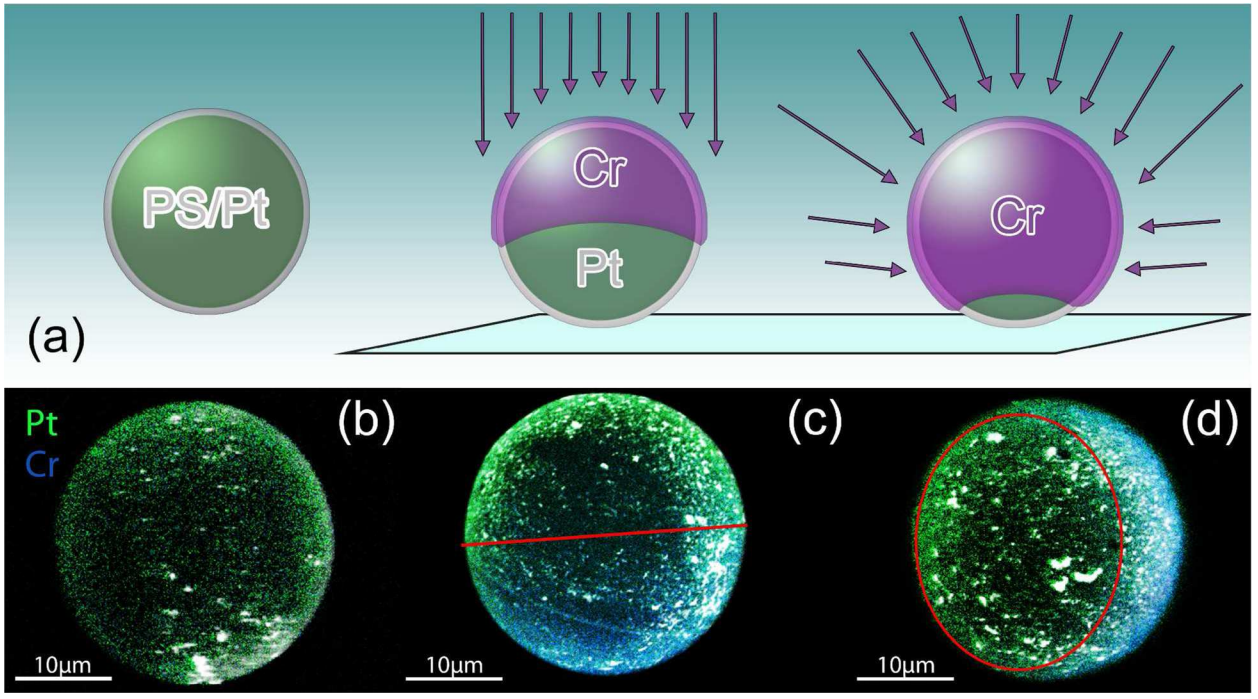

Figure 1. (a) Schematic for the three different bubble swimmer geometries targeted (left to right: symmetrical, Janus, and pore activity); purple arrows indicate directionality of evaporation. E-beam shows strong directionality (middle), while sputter coating is less directional (right). Blue surface indicates glass slide substrate. (b–d) Overlaid EDS images for Pt peak intensity (green, energy range of 1.93–2.17 eV) and Cr peak intensity (blue, energy range of 5.24–5.58 eV) distribution for typical platinum-coated polystyrene colloids: (b) unmasked; (c) masked by Cr evaporation; (d) masked by Cr sputter coating. Red line indicates approximate boundary between the catalytically active and masked regions.

surface flow effects. In order to be able to track the position of the particles during these videos it was necessary to run an image subtraction routine implemented using custom LabVIEW (National Instruments) image analysis algorithms, where successive images were subtracted. This allowed for the lingering bubbles in proximity to the particles current position to be removed, isolating the latest bubble produced by the swimmer. This bubble was then used to track the motion of the particles using a custom-written multiple particle motion tracking algorithm which output 2D x, y trajectory data as a function of time for each particle present in a given video sequence. Before trajectory analysis, simple algorithms were applied to ensure tracks of particles were at least 15 s long and any falsely tracked particles were binned. Average instantaneous velocities were calculated for each trajectory passing these criteria, along with fractal dimension, mean radius of gyration, and persistence length using custom algorithms implementing the analysis described below. Prior to fractal dimension and persistence length determination, Savitzky–Golay smoothing was performed in LabVIEW, with a setting of 5 side-points (k). This filter performs the piece-by-piece fitting of a polynomial to the data using least-squares minimization, where the fitting window has a length of $(2k + 1)$. The Levenburg–Marqaudt function in LabVIEW was used to fit eq 4 to our experimental data to find the persistence length, L_P. Where the trajectory contained loops, the plot of $\langle \cos \theta \rangle$ displayed a sinusoidal pattern; consequently, the fitting of eq 4 was applied to the early exponential decay curve ($L \leq 1$ mm). Binning and averaging of the cos θ data to find L_P relies on the trajectory chain segments having equal step sizes ΔL. To ensure that this was the case the linear interpolation function in LabVIEW was applied to add an additional 20 points between the smoothed trajectory points. Then points ΔL apart were selected from the interpolated data to produce trajectories where the vectors were of equal length. We chose ΔL to be sufficiently small so as to reproduce the smoothed trajectories, see Figure 5B; typically, this would be $\Delta L = L_c/10000$ where L_c is the trajectory contour length.

2.4. Stochastic Model. The simple algorithm to generate model bubble release trajectories was implemented using LabVIEW. The only variable in the algorithm that controls the resulting trajectories is the arc angle, $\ominus$, which limits the range of angles over which translations can occur. Each trajectory step is generated as follows: first a random number generator is used to generate a new bubble release angle, ξ, such that $-\ominus/2 \leq \xi \leq \ominus/2$. This angle is then added to the current colloidal orientation angle, φ (φ defines the orientation of the active portion of the colloid and bisects the arc angle) to determine the angular position of the new bubble release event, $\alpha = \varphi + \xi$. A unit length translation orientated in the opposite direction to α is then applied to the current colloidal x, y coordinates (i.e., $x' = x - \Delta x$ where $\Delta x = \cos \alpha$; and $y' = y - \Delta y$ where $\Delta y = \sin \alpha$). Finally, the new orientation of the active patch is updated according to $\varphi' = \alpha$. This last stage reorients the particles bubble-producing region to be aligned with the randomly chosen bubble release position and is used in the algorithm as a crude proxy for the torques that bubble detachment may generate.

3. RESULTS AND DISCUSSION

3.1. Masking Catalytic Activity. Figure 1a schematically displays the targeted spherical colloid structures investigated here: homogeneous symmetrical catalytic activity, hemispherical Janus activity, and activity localized at a pore with circular perimeter. Nominally symmetrically active catalytic colloids were manufactured by chemically reducing a platinum

DOI: 10.1021/acs.jpcc.5b03773
J. Phys. Chem. C XXXX, XXX, XXX–XXX

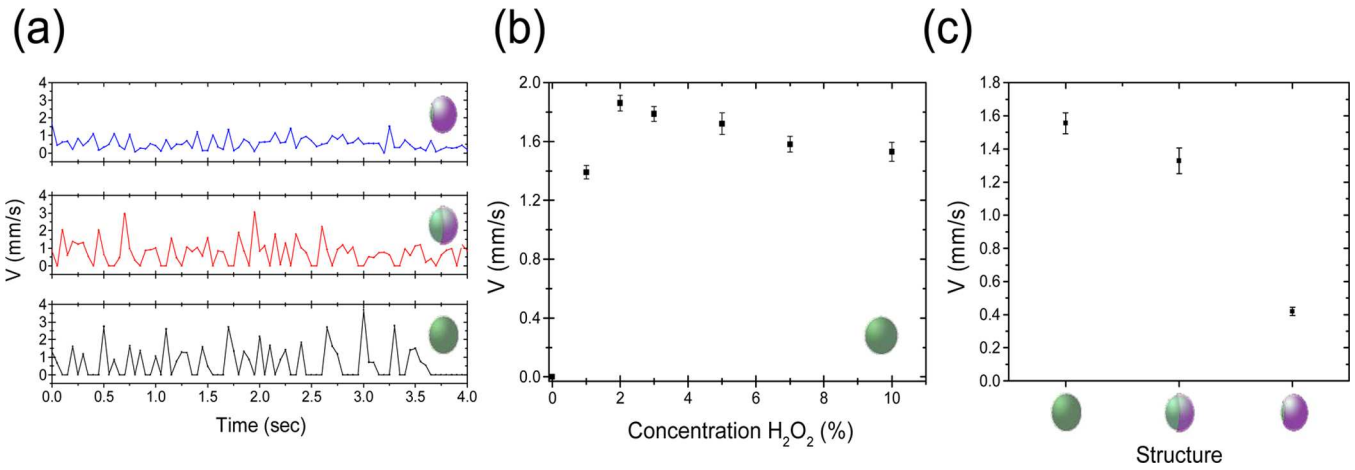

Figure 2. (a) Instantaneous velocity (V) against time for typical pore, Janus, and symmetrical activity catalytic colloids. (b) Mean instantaneous velocity as a function of hydrogen peroxide concentration for the symmetrically active colloid (minimum of 20 measurements). (c) Mean instantaneous velocity as a function of structure (10% w/v H_2O_2; data from 33 symmetrical, 63 Janus, and 246 pore particles).

containing salt onto the surface of 30 μm diameter polystyrene colloids. Figure 1b shows a typical EDS image from such a colloid. A uniform distribution of platinum is revealed across the surface and was confirmed for many colloids. This is consistent with the solution-based platinum reduction proceeding symmetrically across the colloid surface. Reaction rate measurements have demonstrated that a thin overlayer of chromium acts as an effective mask to platinum catalytic activity for hydrogen peroxide decomposition [bare platinum (20 nm) hydrogen peroxide decomposition reaction rate constant = 9.26 $\times$ 10^{10} s^{-1} μm^{-2}; platinum with a 5 nm chromium overlayer deposited by e-beam: reaction rate = 5.97 $\times$ 10^{8} s^{-1} μm^{-2}, a 150 times slower reaction rate, sufficient to prevent bubble generation]. Consequently, we use a second spatially well-defined chromium deposition to impart asymmetry to these initially uniformly catalytically active colloids. To deposit the masking layer, symmetrical colloids were dispersed onto a planar substrate and subject to one of two chromium deposition methods. In the first, chromium was deposited using thermal evaporation, which is known to result in line of sight deposition between the evaporation source and the coated surface. Figure 1c shows EDS maps for a typical colloid produced in this way, which as expected shows a symmetrical Janus structure, with a hemispherical chromium mask deposited. In the second masking approach, the chromium was instead deposited using sputter coating. Sputter coating is less directional, potentially allowing the chromium mask to deposit on the underside of the colloids; however, the lower portion of the colloid in contact with the substrate is still expected to be physically masked. Figure 1d displays an EDS map for a typical sputter-coated colloid, and it is indeed apparent that the exposed platinum region is now pore-shaped, with less than half the spheres' surface exposed. Statistical analysis over several EDS images reveals that the mean circular pore diameter is 23 $\pm$ 2 μm, corresponding to 19% $\pm$ 5% exposed catalytic surface. This would represent an arc angle of 68° $\pm$ 19° in the simple stochastic model described below.

3.2. Bubble Propulsive Behavior. All three catalytically active colloid samples (symmetric, Janus, and pore) were dispersed in Petri dishes containing hydrogen peroxide, and their motion was monitored and recorded using video microscopy. Qualitatively, bubbles could be seen to issue from the colloids surfaces and cause them to undergo enhanced motion (see Supporting Information videos). Image analysis was used to extract x, y coordinates for many individual colloids of each type as a function of time, allowing a range of additional analysis to be performed. Figure 2a shows typical instantaneous velocities as a function of time for the three different active colloid structures in 10% w/v hydrogen peroxide solutions. It is clear that motion proceeds via a stop−start mechanism, reflecting the bubble growth and burst process occurring at the catalytically active surfaces as discussed and modeled elsewhere.[20] Figure 2b displays the effect of varying peroxide concentration on average instantaneous velocity for the symmetrically active colloid in the range of 0−10 wt %/v hydrogen peroxide concentration. Mean instantaneous velocities range from 1.4 to 1.8 mm/s, with maximum propulsion velocity observed at 2% w/v fuel. Increasing the fuel concentration above 2% results in a slow reduction in velocity. However, reaction kinetic experiments show that the rate of peroxide decomposition by platinum continues to increase in the range of 2−10%. These results consequently indicate that the bubble propulsion mechanism is not benefited by this additional gas generation rate. We note that this maximum propulsion velocity is comparable to that produced by similarly sized titanium-masked water-driven swimmers that have an inbuilt Ga/Al alloy fuel source which were reported to move at a maximum velocity of 3 mm/s.[12] However, a key feature for our system is that propulsion was observed in the absence of surfactant, whereas the Ga/Al spheres were observed in solutions containing Triton surfactant. For further comparison, catalytic nanotube swimmers report velocities ranging from 12 to 500 μm/s,[29−38] and Wang and co-workers find peak values at 980 μm/s[39] for PANI/Pt microjets and 1410 μm/s for PEDOT/Pt microjets.[40] Again in each case these jet and rod velocities were reported in surfactant containing solutions.

Figure 2c compares the mean velocity for the three catalyst distributions studied here. The Janus structures' small reduction in velocity compared to the symmetrical geometry suggests bubble generation is more efficiently converted into motion in the case of hemispherical coverage, indicating that spatial control for catalyst distribution may be desirable. The pore-shaped activity colloids exhibit a quarter of the symmetrical propulsion velocity, aligned to the reduction in exposed catalyst area (19% surface activity). An additional feature for the behavior for all three catalyst distributions is differences in their

DOI: 10.1021/acs.jpcc.5b03773
J. Phys. Chem. C XXXX, XXX, XXX−XXX

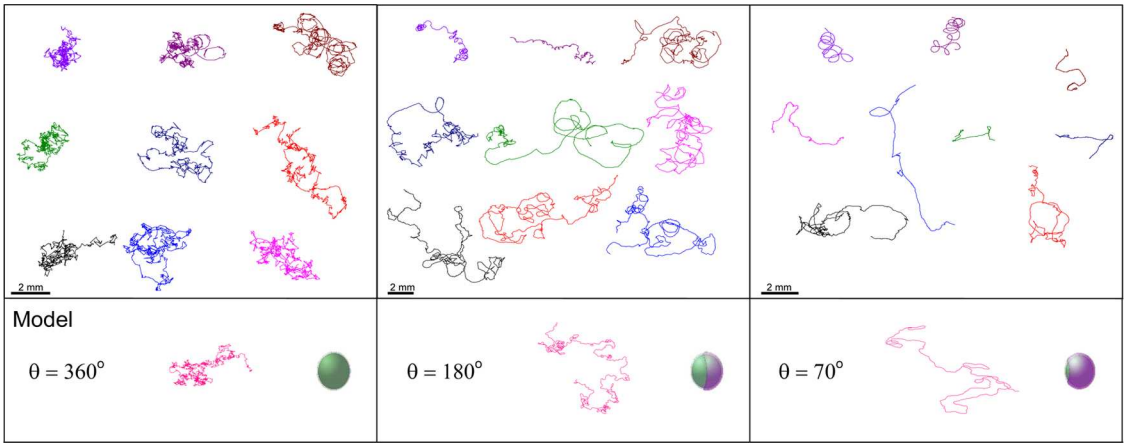

Figure 3. Trajectories of 40 s duration for typical bubble propulsive colloids recorded in 10% w/v hydrogen peroxide (left to right: symmetrical activity, Janus activity, and pore activity). Lower box: trajectories produced using a simple 2D model (see Figure 4) with arc angle chosen to match the geometry of the colloids as determined by EDS (see Figure 1).

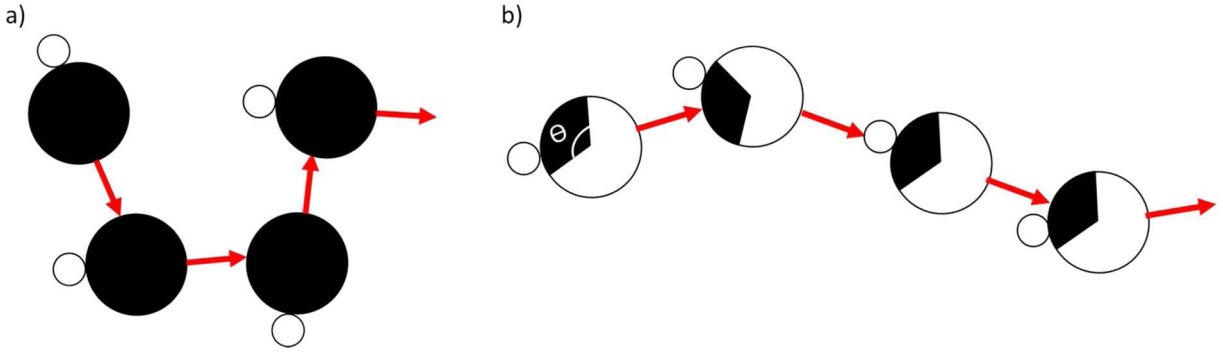

Figure 4. Stochastic model for bubble release: (a) symmetrically coated particle bubble release occurs at a random position on the perimeter of the particle (indicated by the smaller open circle), resulting in translation away from the detachment point; (b) asymmetrical particle with patch defined by arc angle, Θ: motion proceeds as in panel a, but bubble release also produces a torque which is modeled by aligning the catalytic patch with the previous bubble release position. This has the effect of producing increased orientation changes for bubble release at the edges of the arc, and no change for bubble release that is centered within the catalytic arc perimeter.

relative residence times at the air−water interface of the Petri dish compared to times spent executing fully submerged bulk swimming. Unmasked symmetrically active particles were observed to most frequently move within the bulk solution, but did switch back and forth between the bulk and air−water interface, whereas masked particles showed a much higher proportion swimming on the air−water interface, with occasional particles moving into the bulk solution. Observations indicated that particles with pore activity remained at the air−water interface more than colloids with Janus activity. Previous studies have also reported changes in vertical height within a fluid volume for bubble generating devices, which have been explained by buoyancy changes produced by growing surface attached bubbles.[41,42] Further to this we find that the particle detachment energy required for our particles to leave the air−liquid interface (γ_{aw}), assuming gravity is negligible, for a particle radius of a = 15 μm calculated with eq 1 as $E = 1.3 \times 10^{10} kT$, where θ represents the contact angle. This would mean that, considering this factor only, our particles should not be able to detach from the interface.

$$E = \pi a^2 \gamma_{aw} (1 - \cos \theta)^2 \quad (1)$$

However, in reality it appears that, in addition to contributions from gravity and meniscus pinning effects, bubbles may additionally disturb the surface tension to together cause detachment in some cases. Indeed, similar to the observations reported here, previous symmetrically active bubble generating devices were seen to rise to the air−water interface due to increased buoyancy and then either remain at the interface undergoing enhanced motion or sink back down into the bulk after attached bubbles burst.[42] Our data suggests that introducing asymmetry to the catalytic activity enhances residence time at the air−water interface; however, the mechanism for this is unclear.

Having considered the differences in instantaneous propulsion velocity, we now investigate how the translational motion compares between the three geometrically differing catalytic activity distributions, in particular to assess if imparting asymmetry to the catalyst activity correlates with increased directionality of motion.

Figure 3 displays representative trajectories for the three bubble propulsive geometries considered here. It is clear that there is significant diversity in trajectory character for a given catalytic distribution, as can also be seen from the example Supporting Information movies. Within each catalyst distribution, some trajectories appear to show spiralling behavior, in contrast to the remainder that do not have an obvious rotational component. It appears that each of three catalyst geometries can generate rotational motion, and the masking was unable to control this effect. However, despite this,

DOI: 10.1021/acs.jpcc.5b03773
J. Phys. Chem. C XXXX, XXX, XXX−XXX

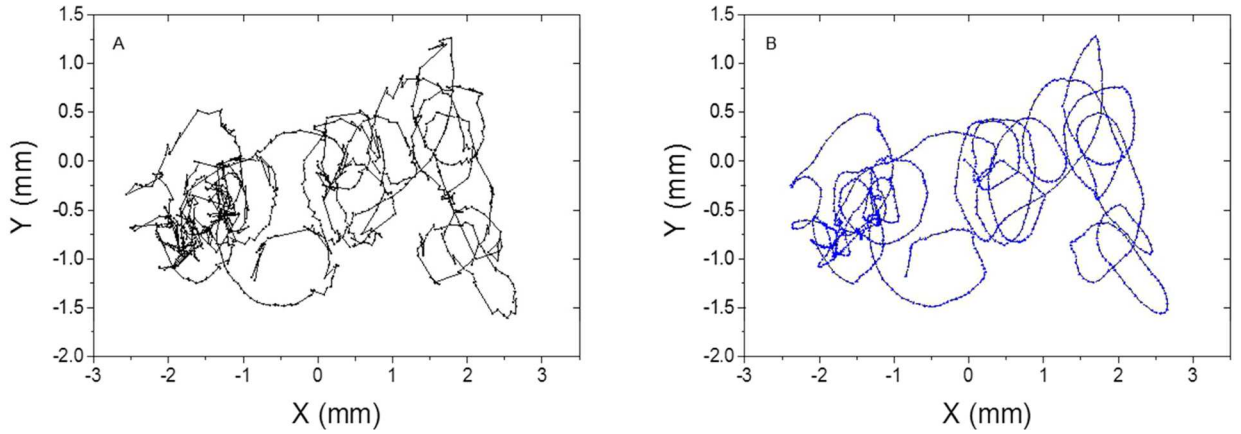

Figure 5. Example of trajectory smoothing performed to allow fractal analysis: (A) original trajectory; (B) trajectory smoothed using Savitzky−Golay smoothing filter.

systematic differences between the three catalyst arrangements can also be qualitatively identified. Despite the symmetrical activity producing the highest mean instantaneous velocity, the associated trajectories show frequent abrupt changes in direction, resulting in smaller average displacement from the starting point compared to the two asymmetrical catalytic activity colloids. A Janus catalytic activity distribution reduces the rapid direction changes, giving rise to smoother trajectories, larger displacements from the origin, and several trajectories with sections as long as 2 mm without significant direction changes. Likewise, with the exception of trajectories that spiral, pore catalytic activity appears to extend this increased trajectory directionality trend further, with one trajectory exhibiting a directed run of around 5 mm. When considering the pore trajectories it should also be borne in mind that this structure is producing significantly slower mean propulsion velocities, but still showing more directional behavior over the same duration trajectory excerpt.

3.3. Simple Stochastic Bubble Release Model. In an attempt to reproduce these qualitative features we have created a simple stochastic model for bubble release trajectories. Figure 4 shows the simplistic stochastic 2D model representation of the motion due to bubble propulsion on a symmetrically coated particle (Figure 4a) and on a masked particle with an exposed catalytically active pore of angle $\ominus$ (Figure 4b).

The model encompasses the idea that bubble release occurs at a random position on the Pt exposed surface, causing the swimming device to move in the opposite direction, Figure 4a. As the catalytic arc available for bubble generation is reduced, the possible directions of motion available to a device starting with an arbitrary orientation are consequently also reduced, Figure 4b. However, this alone does not allow for any reorientation of the partially catalytically active model bubble swimmers with time. To encompass the likely physical situation, that a bubble releasing and growing toward the edge of the arc will also rotate the device, the model also realigns the particles' catalytically active pore orientation to the previous bubble release position. In the case of symmetrical particles this realignment has no effect; however, for devices with a partial arc, reorientation from an initial arbitrary starting alignment now occurs if stochastic bubble release occurs away from the midpoint of the arc, Figure 4b. Typical example trajectories generated from this model, with arc angles matching those found from EDS analysis for the three experimental catalyst distributions, are shown below the experimental trajectories in Figure 3. These trajectories exhibit similar tendencies to the experimental data, explaining how confining the available catalytic surface for bubble generation can impart increased directionality. We note that the microscopic observations we have made are insufficiently clear to reveal the actual distribution of bubble release positions, and so have based this model on the assumption of stochastic bubble distribution over the catalytically active section. If instead, bubble release showed a preference for certain positions at the active surface then an increased persistence of motion would correspondingly be produced.

3.4. Quantitative Analysis for Bubble Swimmer Trajectories. The above qualitative discussion illustrates the difficulty in comparing trajectories for bubble swimming devices, which hampers gaining an understanding of the relationship between catalyst distribution and performance. To address this, here we apply a range of trajectory analysis methods that have proved useful in related complex path problems such as sperm trajectories[43] and protein motor transport[28] to allow quantitative assessment of the above qualitative observations: fractal dimension, radius of gyration, and persistence length.

Fractal dimension D_f is a measure of the space filling properties of an object.[44] Unless the object completely fills the space it occupies, D_f will be smaller than the embedding dimension. Fractal dimension has been used to quantify a wide variety of systems, including aggregating diffusing particles and clusters,[45] particle gels,[46] bacterial colonies,[47] and biopolymer gels.[48] Calculating the fractal dimension of the trajectories of our bubble swimmer particles consequently provides a number by which we can statistically compare behavior. At sufficiently long time scales the 2D trajectory of a sphere displaying simple Brownian diffusion will have a fractal dimension of 2, while the trajectory of a sphere propelling in a straight line has a fractal dimension of 1. To obtain D_f we used a method described by Katz and George for the analysis of growth paths or trails for biological cells and axons moving in 2D.[49] The fractal dimension is given by

$$D_f = \frac{\log(n)}{\log(nd/L)} \quad (2)$$

where n is the number of trajectory segments (equivalent to the number of images in the sequence), d is the planar diameter of the trajectory, and L is the path length. The planar diameter d is

DOI: 10.1021/acs.jpcc.5b03773
J. Phys. Chem. C XXXX, XXX, XXX−XXX

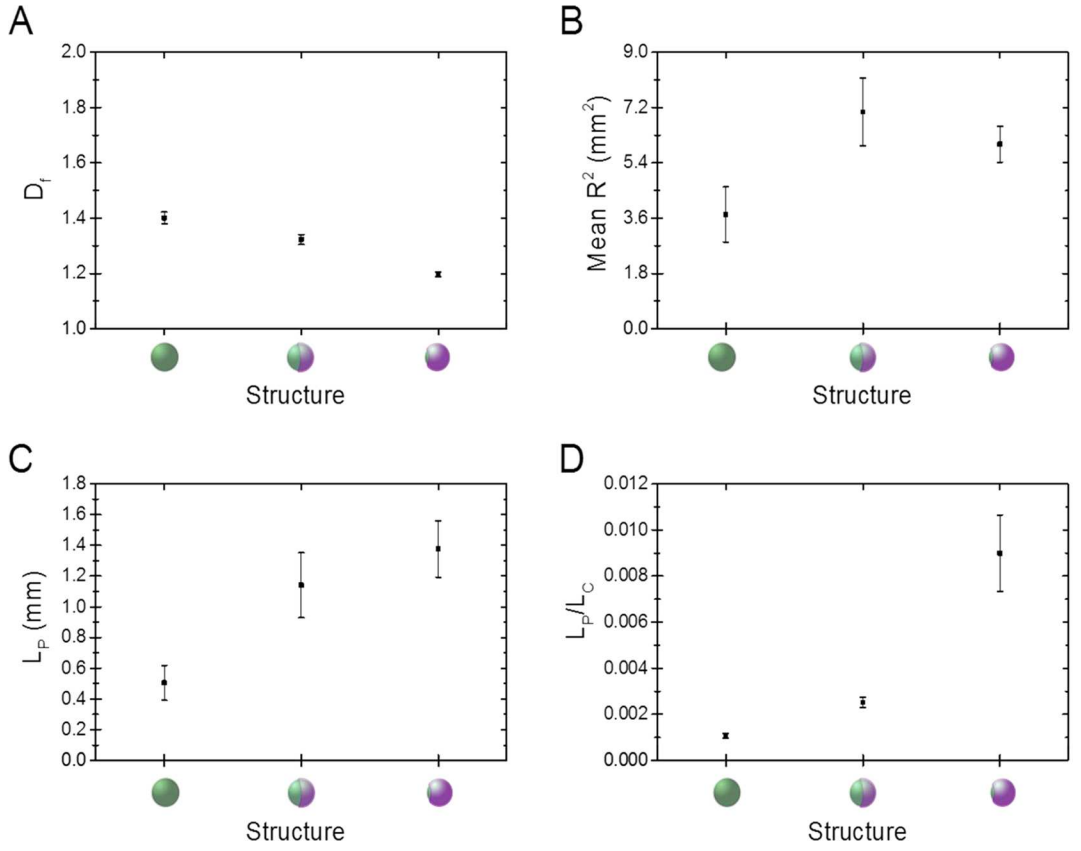

Figure 6. Results of trajectory analysis for bubble swimmers: (A) fractal dimension (D_f); (B) mean-squared radius of gyration (R_g^2); (C) persistence length (L_P). Panel D shows values normalized to total path length (L_C).

found by computing the maximum distance between any two points in the trajectory. As the image analysis algorithms that we used to extract the trajectories follow the bubbles formed on the surface of the swimmer particle, random fluctuations in the tracking of the swimmers is introduced. By smoothing the data we remove those random fluctuations which can artificially inflate D_f and follow the core trajectory of the swimmer particle. This was performed using Savitzky−Golay smoothing: piece-by-piece fitting of a polynomial to the data using least-squares minimization, Figure 5.

Figure 6A shows that symmetrical activity colloids produce trajectories with a mean fractal dimension of 1.40, Janus activity produces a modest reduction in fractal dimension compared to the symmetrical activity case, and that pore-shaped catalytic activity produces a further reduction. This suggests that confining the surface region displaying catalytic activity can produce less recursive trajectories, which in turn will be more useful for transport applications. One advantage for fractal analysis is that it provides a dimensionless result, and so can allow comparison for motion produced over a variety of length and time scales. For example, the fractal dimension for self-motile sperm has been reported to be around 1.3, similar to that observed for the Janus bubble swimmer here.[43] In contrast, the other two analysis methods applied report length scales, which, without normalization, reflect both propulsion velocity and directionality differences.

Mean-squared radius of gyration, R_g^2, calculates the average mean-squared distance of each point on a trajectory from a defined central fixed point, and so reflects how compact or spread out in space a given trajectory segment is. Here we calculate R_g^2 using eq 3, in analogy to the definition used for polymer chain analysis.

$$R_g^2 = \frac{1}{N}\sum_{i=1}^{N}(r_i - r_{mean})^2 \quad (3)$$

In our application, r_{mean} is chosen to be the mean position for the trajectory (i.e., the unweighted mean x, y coordinate for the trajectory segment). Mean-squared gyration values are also seen to increase for both Janus and pore activity distributions relative to the lower value for symmetrical activity devices, Figure 6B. Larger values for mean-squared gyration values reflect trajectories that on average extend over larger regions of space. When compared for a fixed duration trajectory, as presented here, this can indicate either a more directed motion or faster transport. Figure 2c shows that both the asymmetrical catalyst distribution swimmers show lower propulsion velocities, significantly so for the pore activity example, and so the increase in radius of gyration provides additional evidence that confining the catalyst active area is resulting in more directed motion and longer distance transport.

Finally we consider the use of persistence length measurements. Often used as a measure of the stiffness or bending properties of a polymer chain, the persistence length, L_P, denotes the distance along a set of chain segments where the correlation of the angle θ between segment vectors is lost, i.e., a linear set of chain segments will result in a larger L_P than a set of chain segments featuring curves or loops. It has been applied to a variety of systems including man-made polymers, biopolymers,[50] and in the characterization of the trajectories of microtubules moving on a kinesin-coated surface.[28] Again,

DOI: 10.1021/acs.jpcc.5b03773
J. Phys. Chem. C XXXX, XXX, XXX−XXX

without normalization this analysis will reflect both velocity and directionality.

Our bubble swimmer trajectories are a chain of vectors. We determined L_P for each trajectory by first computing the average cosine angle $\langle \cos \theta \rangle$ between vectors at all separation distances L along the chain. This was done by superimposing vectors at position j on the vector at starting position i and calculating cos θ, where $j \geq i$ and i represents all starting positions along the chain (see Figure 7). For our 2D trajectories a plot of $\langle \cos \theta \rangle$ against separation distance $L = \Delta L(j - i)$ has the form

$$\langle \cos \theta \rangle = e^{-(L/2L_P)} \quad (4)$$

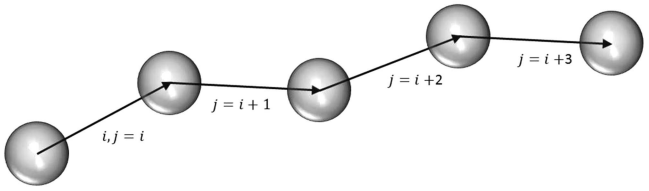

Figure 7. Bubble swimmer trajectories are a chain of vectors. The persistence length is found by computing the average cos θ between the starting vector at position i and the superimposed vectors at position j, for all separation distances $L = \Delta L(j - i)$ along the chain and all starting positions i.

Figure 6C shows that persistence length determined in this way is increased significantly from 0.5 to 1.1 mm by changing from uniform catalytic activity to Janus activity. Persistence length further increases to 1.4 mm with decreasing activity site size (pore size), despite the large accompanying reduction in propulsion velocity. Persistence lengths can also be normalized to express the persistence as a fraction of the total path length, Figure 6D. This measure allows assessment of the catalyst distribution on directionality irrespective of propulsion velocity and shows that the pore-shaped geometry results in a persistence length roughly 10 times that of the symmetrical case and 5 times that of the Janus structure. Taken together it is clear that these analysis methods are able to reveal statistically significant differences across groups of widely varying trajectories such as those shown in Figure 3, without making assumptions about the link between device orientation and propulsion direction.

Figure 8 shows results for similar fractal and persistence length analysis for many trajectories generated from the simple stochastic model introduced above. The fractal dimension data reproduces the decrease in fractal dimension with reducing pore arc observed experimentally and also shows a significant increase in relative persistence length for smaller pores. This suggests that engineering devices with highly localized bubble generation sites could further extend the trajectory control experimentally found here.

To illustrate the character of motion produced by these spherical bubble swimmers, it is instructive to calculate their expected persistence length, assuming that device orientation determines translational thrust direction and the body of the swimming device is solely reorientated by Brownian rotational diffusion. In this case the persistence length is estimated to be the product of the Brownian rotational diffusion time constant (2100 s) and the propulsion velocity, yielding a length of 8.4 m. It is abundantly clear that the observed behavior is nowhere near this directional, with the pore catalytic activity sample achieving only 0.015% of this persistence. For comparison, it is also interesting to consider the case for phoretic Janus swimmers, where a well-defined link between orientation and propulsion direction does exist. For the case of a 5 μm diameter Janus phoretic swimmer, producing a plausible propulsion velocity of 5 μm s^{-1}, the expected persistence length is approximately 0.5 mm, and indeed this agrees with experimental trajectories.[23] The ability for such a device moving at only 1% of the propulsion velocity of a bubble swimmer to produce similar order of magnitude persistence length provides further evidence for the highly chaotic nature of bubble release, and the associated rapid trajectory randomization, even for devices with spatially well-defined activity. The significant additional loss of directionality for bubble propulsive devices could be due to two factors: enhanced device rotation rate due to the bubble propulsion process (i.e., driven rotations) and poor correlation between device orientation and subsequent propulsion direction. Without direct high-resolution, high frame rate observation to reveal the orientation of the catalyst patch during motion, assessing these two factors is difficult. However, it is clear that controlling the distribution of catalyst can contribute to reducing trajectory randomization factors. The simple stochastic model for bubble release contains two features that together qualitatively reproduce the experimental trends, Figure 3. In this model, directionality arises because confining bubble release to a smaller region of the devices surface enhances the chance of motion continuing

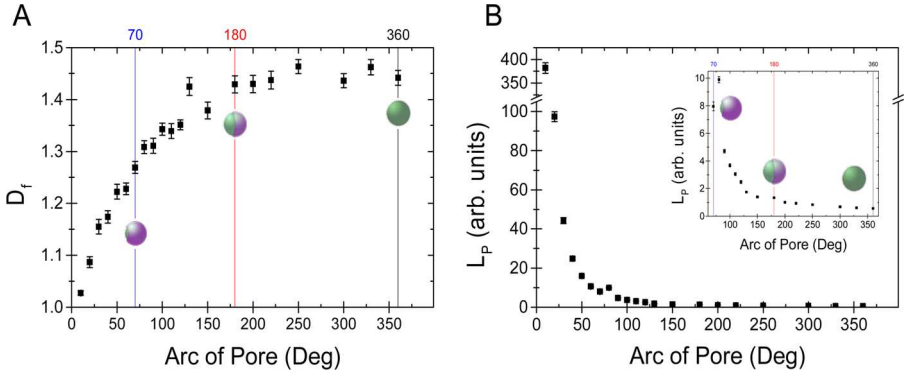

Figure 8. Trajectory analysis for model data generated for different exposed catalytic surface coverages: (A) fractal dimension; (B) persistence length; inset shows enlarged region between the arc angle of 60° and 360°. Vertical lines show region of experimental data.

DOI: 10.1021/acs.jpcc.5b03773
J. Phys. Chem. C XXXX, XXX, XXX−XXX

in the current direction and reduces the chance of significant rotational torque being associated with bubble release.

4. CONCLUSIONS

We have systematically investigated the effect of varying the surface catalytic activity distribution on the trajectories for bubble propelled spherical swimmers. A simple symmetric spherical catalyst particle produces high mean instantaneous velocities in the presence of fuel (1.8 mm s^{-1}); however, qualitatively the trajectories show frequent changes in direction. By comparison, a sphere with Janus catalyst distribution shows slightly reduced propulsion velocity, but more directional trajectories. If activity is constrained to a pore, directionality is further enhanced, but with a significant reduction in propulsion velocity. To aid quantitative comparison between these geometries, and to develop and test general methods to analyze propulsive device motion, we illustrate how fractal dimension, radius of gyration, and persistence length calculations can statistically compare many disparate trajectories. These measures confirm that constraining catalytic activity to a more localized region on the bubble-producing devices surface results in a more directed, less recursive trajectory, with a lower fractal dimension, and in addition significantly increases persistence length and extends the radius of gyration.

However, it is clear that bubble propulsion introduces an extremely high degree of randomization to the trajectories, in contrast to phoretic swimmers that have been reported to produce persistence lengths limited only by Brownian rotational diffusion. A simple stochastic model demonstrating how catalytic activity distribution can alter trajectories by confining bubble release location and reducing the changes in orientation associated with bubble release and growth illustrates the possible origins of the behavior observed for these bubble swimmers.

In the wider context of swimming device research, we have demonstrated that, if applied appropriately, fractal dimension analysis and persistence length measurements provide a valuable tool in comparing trajectory character between disparate motion producing species including biological swimmers at different lengths scales and synthetic devices. It is hoped that this study may promote the use of these measures across the swimming device field, particularly for other bubble propulsive devices such as nanotube "rockets",[51] where quantification of trajectory character has so far received little attention. Applying consistent quantitative analysis can also aid future selection of devices with trajectories most appropriate to a given task and allow benchmarking for the various proposed approaches to autonomous motion generation at small scales.

■ ASSOCIATED CONTENT

Supporting Information

Video 1, symmetrically active colloids in 10% w/v hydrogen peroxide fuel, video 2, Janus-active colloids in 10% w/v hydrogen peroxide fuel, and video 3, pore-active colloids in 10% w/v hydrogen peroxide fuel. The Supporting Information is available free of charge on the ACS Publications website at DOI: 10.1021/acs.jpcc.5b03773.

■ AUTHOR INFORMATION

Corresponding Author

*E-mail: s.ebbens@sheffield.ac.uk.

Author Contributions

The manuscript was written through contributions of all authors. All authors have given approval to the final version of the manuscript.

Notes

The authors declare no competing financial interest.

■ ACKNOWLEDGMENTS

We acknowledge support from the EPSRC via S. Ebbens Career Acceleration Fellowship (EP/J002402/1).

■ REFERENCES

(1) Gao, W.; Dong, R.; Thamphiwatana, S.; Li, J.; Gao, W.; Zhang, L.; Wang, J. Artificial Micromotors in the Mouse's Stomach: A Step toward in Vivo Use of Synthetic Motors. *ACS Nano* **2015**, *9* (1), 117−123.

(2) Baraban, L.; Tasinkevych, M.; Popescu, M. N.; Sanchez, S.; Dietrich, S.; Schmidt, O. G. Transport of Cargo by Catalytic Janus Micro-Motors. *Soft Matter* **2012**, *8*, 48−52.

(3) Najafi, A.; Golestanian, R. Simple Swimmer at Low Reynolds Number: Three Linked Spheres. *Phys. Rev. E* **2004**, *69* (6), 062901.

(4) Ebbens, S. J.; Howse, J. R. In Pursuit of Propulsion at the Nanoscale. *Soft Matter* **2010**, *6* (4), 726.

(5) Wang, W.; Duan, W.; Ahmed, S.; Mallouk, T. E.; Sen, A. Small Power: Autonomous Nano- and Micromotors Propelled by Self-Generated Gradients. *Nano Today* **2013**, *8* (5), 531−554.

(6) Kapral, R. Perspective: Nanomotors without Moving Parts That Propel Themselves in Solution. *J. Chem. Phys.* **2013**, *138* (2), 020901.

(7) Solovev, A. A.; Xi, W.; Gracias, D. H.; Harazim, S. M.; Deneke, C.; Sanchez, S.; Schmidt, O. G. Self-Propelled Nanotools. *ACS Nano* **2012**, *6* (2), 1751−1756.

(8) Gibbs, J. G.; Zhao, Y.-P. Autonomously Motile Catalytic Nanomotors by Bubble Propulsion. *Appl. Phys. Lett.* **2009**, *94* (16), 163104.

(9) Soler, L.; Martínez-cisneros, C.; Swiersy, A.; Sánchez, S.; Schmidt, O. G. Thermal Activation of Catalytic Microjets in Blood Samples Using Microfluidic Chips. *Lab Chip* **2013**, *13* (22), 4299−4303.

(10) Vicario, J.; Eelkema, R.; Browne, W. R.; Meetsma, A.; La Crois, R. M.; Feringa, B. L. Catalytic Molecular Motors: Fuelling Autonomous Movement by a Surface Bound Synthetic Manganese Catalase. *Chem. Commun.* **2005**, No. 31, 3936−3938.

(11) Gao, W.; D'Agostino, M.; Garcia-Gradilla, V.; Orozco, J.; Wang, J. Multi-Fuel Driven Janus Micromotors. *Small* **2013**, *9*, 467−471.

(12) Gao, W.; Pei, A.; Wang, J. Water-Driven Micromotors. *ACS Nano* **2012**, *6* (9), 8432−8438.

(13) Li, J.; Singh, V. V.; Sattayasamitsathit, S.; Orozco, J.; Kaufmann, K.; Dong, R.; Gao, W.; Jurado-sanchez, B.; Fedorak, Y.; Wang, J.; et al. Water-Driven Micromotors for Rapid Photocatalytic Degradation of Biological and Chemical Warfare Agents. *ACS Nano* **2014**, *11* (8), 11118−11125.

(14) Wang, S.; Wu, N. Selecting the Swimming Mechanisms of Colloidal Particles: Bubble Propulsion versus Self-Diffusiophoresis. *Langmuir* **2014**, *30*, 3477−3486.

(15) Gao, W.; Feng, X.; Pei, A.; Gu, Y.; Li, J.; Wang, J. Seawater-Driven Magnesium Based Janus Micromotors for Environmental Remediation. *Nanoscale* **2013**, *5*, 4696−4700.

(16) Simmchen, J.; Baeza, A.; Ruiz, D.; Esplandiu, M. J.; Vallet-Regí, M. Asymmetric Hybrid Silica Nanomotors for Capture and Cargo Transport: Towards a Novel Motion-Based DNA Sensor. *Small* **2012**, *8* (13), 2053−2059.

(17) Golestanian, R.; Liverpool, T. B.; Ajdari, A. Designing Phoretic Micro- and Nano-Swimmers. *New J. Phys.* **2007**, *9* (5), 126−126.

(18) Ebbens, S.; Gregory, D. A.; Dunderdale, G.; Howse, J. R.; Ibrahim, Y.; Liverpool, T. B.; Golestanian, R. Electrokinetic Effects in Catalytic Platinum-Insulator Janus Swimmers. *Europhys. Lett.* **2014**, *106* (5), 58003.

DOI: 10.1021/acs.jpcc.5b03773
J. Phys. Chem. C XXXX, XXX, XXX−XXX

(19) Howse, J.; Jones, R.; Ryan, A.; Gough, T.; Vafabakhsh, R.; Golestanian, R. Self-Motile Colloidal Particles: From Directed Propulsion to Random Walk. *Phys. Rev. Lett.* **2007**, *99* (4), 8−11.
(20) Manjare, M.; Yang, B.; Zhao, Y. P. Bubble Driven Quasioscillatory Translational Motion of Catalytic Micromotors. *Phys. Rev. Lett.* **2012**, *109*, 1−5.
(21) Fletcher, N. H. Size Effect in Heterogeneous Nucleation. *J. Chem. Phys.* **1958**, *29*, 572.
(22) Ebbens, S. J.; Howse, J. R. Direct Observation of the Direction of Motion for Spherical Catalytic Swimmers. *Langmuir* **2011**, *27* (20), 12293−12296.
(23) Ebbens, S.; Tu, M.-H.; Howse, J. R.; Golestanian, R. Size Dependence of the Propulsion Velocity for Catalytic Janus-Sphere Swimmers. *Phys. Rev. E: Stat., Nonlinear, Soft Matter Phys.* **2012**, *85* (2), 020401.
(24) Dunderdale, G.; Ebbens, S.; Fairclough, P.; Howse, J. The Importance of the Mean-Squared Displacement in Distinguishing Nanopropulsion. *Langmuir* **2012**, *28* (30), 10997−11006.
(25) Ebbens, S.; Jones, R. A. L.; Ryan, A. J.; Golestanian, R.; Howse, J. R. Self-Assembled Autonomous Runners and Tumblers. *Phys. Rev. E* **2010**, *82* (1), 6−9.
(26) Wang, H.; Zhao, G.; Pumera, M. Beyond Platinum: Bubble-Propelled Micromotors Based on Ag and MnO2 Catalysts. *J. Am. Chem. Soc.* **2014**, *136*, 2719−2722.
(27) Wilson, D. A.; de Nijs, B.; van Blaaderen, A.; Nolte, R. J. M.; van Hest, J. C. M. Fuel Concentration Dependent Movement of Supramolecular Catalytic Nanomotors. *Nanoscale* **2013**, *5* (4), 1315−1318.
(28) Van Den Heuvel, M. G. L.; Bolhuis, S.; Dekker, C. Persistence Length Measurements from Stochastic Single-Microtubule Trajectories. *Nano Lett.* **2007**, *7*, 3138−3144.
(29) Solovev, A. A.; Sanchez, S.; Pumera, M.; Mei, Y. F.; Schmidt, O. G. Magnetic Control of Tubular Catalytic Microbots for the Transport, Assembly, and Delivery of Micro-Objects. *Adv. Funct. Mater.* **2010**, *20* (15), 2430−2435.
(30) Sanchez, S.; Solovev, A. A.; Schulze, S.; Schmidt, O. G. Controlled Manipulation of Multiple Cells Using Catalytic Microbots. *Chem. Commun.* **2011**, *47* (2), 698−700.
(31) Balasubramanian, S.; Kagan, D.; Hu, C.-M. J.; Campuzano, S.; Lobo-Castanon, M. J.; Lim, N.; Kang, D. Y.; Zimmerman, M.; Zhang, L.; Wang, J. Micromachine-Enabled Capture and Isolation of Cancer Cells in Complex Media. *Angew. Chem., Int. Ed.* **2011**, *50* (18), 4161−4164.
(32) Orozco, J.; Campuzano, S.; Kagan, D.; Zhou, M.; Gao, W.; Wang, J. Dynamic Isolation and Unloading of Target Proteins by Aptamer-Modified Microtransporters. *Anal. Chem.* **2011**, *83*, 7962−7969.
(33) Campuzano, S.; Orozco, J.; Kagan, D.; Guix, M.; Gao, W.; Sattayasamitsathit, S.; Claussen, J. C.; Merkoci, A.; Wang, J. Bacterial Isolation by Lectin-Modified Microengines. *Nano Lett.* **2012**, *12* (1), 396−401.
(34) Gao, W.; Uygun, A.; Wang, J. Hydrogen-Bubble-Propelled Zinc-Based Microrockets in Strongly Acidic Media. *J. Am. Chem. Soc.* **2012**, *134* (2), 897−900.
(35) Zhao, G.; Wang, H.; Khezri, B.; Webster, R. D.; Pumera, M. Influence of Real-World Environments on the Motion of Catalytic Bubble-Propelled Micromotors. *Lab Chip* **2013**, *13* (15), 2937−2941.
(36) Sanchez, S.; Solovev, A. A.; Harazim, S. M.; Schmidt, O. G. Microbots Swimming in the Flowing Streams of Microfluidic Channels. *J. Am. Chem. Soc.* **2011**, *133* (4), 701−703.
(37) Kuralay, F.; Sattayasamitsathit, S.; Gao, W.; Uygun, A.; Katzenberg, A. Self-Propelled Carbohydrate-Sensitive Microtransporters with Built-in Boronic-Acid Recognition for Isolating Sugars and Cells. *J. Am. Chem. Soc.* **2012**, *134*, 15217−15220.
(38) Sanchez, S.; Ananth, A. N.; Fomin, V. M.; Viehrig, M.; Schmidt, O. G. Superfast Motion of Catalytic Microjet Engines at Physiological Temperature. *J. Am. Chem. Soc.* **2011**, *133* (38), 14860−14863.
(39) Gao, W.; Sattayasamitsathit, S.; Orozco, J.; Wang, J. Efficient Bubble Propulsion of Polymer-Based Microengines in Real-Life Environments. *Nanoscale* **2013**, *5* (19), 8909−8914.
(40) Gao, W.; Sattayasamitsathit, S.; Orozco, J.; Wang, J. Highly Efficient Catalytic Microengines: Template Electrosynthesis of Polyaniline/Platinum Microtubes. *J. Am. Chem. Soc.* **2011**, *133* (31), 11862−11864.
(41) Reddy, N. K.; Clasen, C. Self-Propelling Micro-Disks. *Korea-Australia Rheol. J.* **2014**, *26* (1), 73−79.
(42) Agrawal, A.; Dey, K. K.; Paul, A.; Basu, S.; Chattopadhyay, A. Chemical Locomotives Based on Polymer Supported Catalytic Nanoparticles. *J. Phys. Chem. C* **2008**, *112* (8), 2797−2801.
(43) Mortimer, S. T.; Swan, M. A.; Mortimer, D. Fractal Analysis of Capacitating Human Spermatozoa. *Hum. Reprod.* **1996**, *11* (5), 1049−1054.
(44) Mandelbrot, B. B. The Fractal Geometry of Nature. *Am. J. Phys.* **1983**, *51*, 286.
(45) Witten, T. A.; Sander, L. M. Diffusion-Limited Aggregation, A Kinetic Critical Phenomenon. *Phys. Rev. Lett.* **1981**, *47* (19), 1400−1403.
(46) Poon, W. C. K.; Pirie, A. D.; Pusey, P. N. Gelation in Colloid-Polymer Mixtures. *Faraday Discuss.* **1995**, *101*, 65.
(47) Vicsek, T.; Cserző, M.; Horváth, V. K. Self-Affine Growth of Bacterial Colonies. *Phys. A (Amsterdam, Neth.)* **1990**, *167* (2), 315−321.
(48) Takahashi, A.; Kita, R.; Shinozaki, T.; Kubota, K.; Kaibara, M. Real Space Observation of Three-Dimensional Network Structure of Hydrated Fibrin Gel. *Colloid Polym. Sci.* **2003**, *281* (9), 832−838.
(49) Katz, M. J.; George, E. B. Fractals and the Analyisis of Growth Paths. *Bull. Math. Biol.* **1985**, *47* (l), 273−286.
(50) Li, D. C.; Banon, S.; Biswal, S. L. Bending Dynamics of DNA-Linked Colloidal Particle Chains. *Soft Matter* **2010**, *6* (17), 4197−4204.
(51) Kagan, D.; Campuzano, S.; Balasubramanian, S.; Kuralay, F.; Flechsig, G. U.; Wang, J. Functionalized Micromachines for Selective and Rapid Isolation of Nucleic Acid Targets from Complex Samples. *Nano Lett.* **2011**, *11*, 2083−2087.

DOI: 10.1021/acs.jpcc.5b03773
J. Phys. Chem. C XXXX, XXX, XXX−XXX